Polymer Testing 78 (2019) 105932

Contents lists available at ScienceDirect

Polymer Testing

journal homepage: www.elsevier.com/locate/polytest

Material Properties

Enhanced elastomer toughness and fracture properties imparted by chemically reactive flat nanoparticles

Malavarayan Sankarasubramanian[a,b,e,1], Monavareh Torabizadeh[c,1], Zackary A. Putnam[a,b], John C. Moosbrugger[c], Ming Y. Huang[d], Sitaraman Krishnan[a,*]

[a] Department of Chemical and Biomolecular Engineering, Clarkson University, Potsdam, NY, 13699, USA
[b] Materials Science and Engineering Ph.D. Program, Clarkson University, Potsdam, NY, 13699, USA
[c] Department of Mechanical and Aeronautical Engineering, Clarkson University, Potsdam, NY, 13699, USA
[d] Baker Hughes, a GE Company, Houston, TX, 77073, USA
[e] Presently at Intel Corporation, Chandler, AZ, 85226, USA

ARTICLE INFO

Keywords:
Fracture resistance
Filler aspect ratio
Glass transition activation energy
Mullins effect
Viscous dissipation
Co-network formation

ABSTRACT

A remarkable enhancement in the mechanical and fracture properties of elastomers, imparted by flat predominantly 2-dimensional nanoparticles, is reported. Elastomers of hydrogenated nitrile butadiene rubber (HNBR), incorporating surface-functionalized montmorillonite clay, nanographite, carbon fiber, or carbon black, were thermally crosslinked in the presence of a bismaleimide coagent using a peroxide free-radical generator. Clay platelets, side-functionalized with octadecyl amine and edge-functionalized with reactive amino groups, were used to achieve good dispersion in the elastomer matrix. The clay-filled elastomer exhibited multiple glass transitions in their dynamic mechanical analysis (DMA) and approx. 6 times higher tear resistance, 4× higher rubbery plateau modulus, 2× higher modulus of toughness, and 2× higher crack initiation resistance than an elastomer containing equivalent carbon black concentration. Nanographite also resulted in property enhancement, albeit to a lower extent than nanoclay. Flat fillers are evidently able to arrest crack growth better than fillers with spherical or elongated shapes. DMA loss tangent data, and dissipated energy fraction calculated from the cyclic tensile test data, show that the flat fillers are better able to release strain energy in the form of viscous dissipation, rather than use it for increasing the crack surface area. SEM images of fractured surfaces are reported and discussed.

1. Introduction

Fracture strength is an essential requirement for the use of elastomers in the chemical industry, and transportation and aerospace applications. Consequently, there is renewed interest in improving the fracture toughness of elastomers using particulate fillers [1–7], based on a concept dating back to the time when carbon black was being studied for mechanical reinforcement of elastomers [8].

The influence of filler aspect ratio (defined as the ensemble average of the ratio of the largest to the smallest dimension of a particle) on mechanical properties of polymer nanocomposites is well-recognized [6]. However, there are contradictory reports in the literature on the benefits of the use of non-spherical filler particles over carbon black or silica, and studies on elucidating filler shape and size effects are of continued importance [9–14]. Scotti et al. [14] investigated composites of styrene-butadiene rubber (SBR) consisting of spherical and anisotropic silica nanoparticles and found that the rod-like particles (with higher aspect ratio) provided stronger mechanical reinforcement. Zhong et al. [10], who studied SBR nanocomposites with spherical silica particles, elongated halloysite nanotubes, and flat montmorillonite (Mt), reported better reinforcing effect with the spherical particles. Dong et al. [11] compared nanocomposites of natural rubber with carbon black (CB, spherical), graphene oxide (planar), and carbon nanotubes (CNTs, high aspect ratio) and reported that it was the spherical CB that resulted in the best quasi-static fracture resistance and dynamic crack growth resistance. Nadiv et al. [9] compared fracture toughness of an epoxy resin reinforced with 1-D carbon nanotubes, 2-D graphite nanoplatelets, and 3-D graphite particles, and concluded that CNTs exhibited the highest reinforcement efficiency (defined as the ratio of % enhancement and wt % of filler in the composite). They also reported a

* Corresponding author.
E-mail address: skrishna@clarkson.edu (S. Krishnan).
[1] These authors contributed equally.

https://doi.org/10.1016/j.polymertesting.2019.105932
Received 17 April 2019; Received in revised form 30 May 2019; Accepted 10 June 2019
Available online 18 June 2019
0142-9418/

non-monotonic dependence of fracture toughness on nanoparticle concentration, with rather low concentrations at which the fracture toughness peaked.

There are few reports on the use of nanoparticles with reactive surfaces for enhancing fracture toughness of elastomer nanocomposites. In the study reported herein, a dramatic improvement in several mechanical and fracture properties of partially hydrogenated poly(acrylonitrile-*co*-butadiene) rubber (HNBR) was observed when surface-functionalized clay nanoparticles, which contained not only the alkyl groups commonly used to make surfaces of clay platelets nonpolar (and therefore miscible with nonpolar polymers) but also amino groups that were reactive toward a bismaleimide coagent, were incorporated as fillers. A comparison of the properties of the clay-filled elastomer with those filled with conventional carbon black and graphite particles, which did not contain reactive surface amino groups, enabled some direct inferences on the effects of filler shape and interfacial chemistry on elastomer properties.

Several studies have been conducted to understand the effects of filler shape and surface chemistry on the tensile, thermal, and dynamic mechanical properties of elastomers [1–7,9–11,14]. However, investigations focusing on filler interfacial aspects in tandem with the fracture properties of elastomer nanocomposites are limited. How the shape, connectivity, and surface chemistry of the filler particles affect crack initiation and crack propagation in rubbery materials is an important question that requires further analysis. Similarly, how various filler interfaces increase or lower hysteresis in the stress − strain behaviors of elastomer nanocomposites requires additional empirical and theoretical understanding. Some of these questions were addressed in the present study by quantitative characterization of crack initiation and crack propagation of elastomers incorporating four different filler particles. An adaptation of the concept of strain energy release rate that applies to non-glassy materials, in which elastic crack-tip deformation complicates fracture analysis compared with a glassy polymer, was used [15]. The effects of cyclic loading and unloading (in tension) on hysteresis damping of the elastomer nanocomposites were also measured and analyzed in terms of the fraction of strain energy dissipated by viscous losses. A relationship was observed between the measured fracture properties and dissipated energy fractions.

2. Experimental section

2.1. Materials

Hydrogenated nitrile butadiene rubber (HNBR, CAS No. 9003-18-3, Zetpol 2020, Zeon Chemicals), having an acrylonitrile content of 36.25 wt %, iodine value of 28 g per 100 g, and a Mooney viscosity, ML (1 + 4), of 78 at 100 °C was used as the elastomer. Carbon black (N550, Continental Carbon Company, Houston, Texas, oil absorption number 92 $cm^3\ mg^{-1}$, iodine number 12.1 g per 100 g), nanographite (NG, Nano24, Asbury Carbons, New Jersey, 350 $m^2\ g^{-1}$ surface area), and carbon fiber (CF, AGM-94, Asbury Carbons, Asbury, New Jersey) were the three different carbon fillers investigated. Nanomer I.31 PS surface-functionalized clay nanoparticles (nanoclay, NC) were received from Nanocor, Inc. (Hoffman Estates, Illinois). α,α′-Bis(*tert*-butylperoxy)-*m*/*p*-diisopropylbenzene (BBIPB, VUL-CUP 40 KE, Arkema Inc., Philadelphia, Pennsylvania) was used as the peroxide vulcanization agent. The peroxide was a mixture of *meta* and *para* isomers (approx. 3.6:1 ratio), with a melting point in the range of 35–45 °C. For ease of handling, it was supplied in powder form, supported on organosilane-treated calcined kaolin clay (Burgess KE). The BBIPB concentration in the clay mixture was 40 wt %. *N,N′-m*-phenylene bismaleimide (*m*-PBM, CAS No. 3006-93-7, HVA-2) was used as the coagent in the rubber formulations. 4,4′-Bis(α,α-dimethylbenzyl)diphenylamine (CAS No. 10081-67-1, Naugard 445) was used as the antioxidant. Zinc oxide and stearic acid were purchased from Akrochem Corporation (Akron, Ohio).

2.2. Methods

HNBR composites were compounded using a 1.6-L mixing volume laboratory internal rotor mixer (Kobelco Stewart Balling Inc.) equipped with a 30-HP variable speed motor. A two-step process, wherein the polymer, filler, and other ingredients listed in Table 1, except the VUL-CUP 40 KE vulcanization agent, were mixed in the first pass. The first pass mixing was at a rotor speed in the range of 90–100 rpm and a maximum temperature of approx. 105 °C. After dropping and cooling the blend on a two-roll mill, the peroxide vulcanization agent was mixed in the second pass, at a rotor speed of 65–75 rpm and a drop temperature of approx. 85 °C. The resulting blend was pressed into sheets using the two-roll mill and finally vulcanized for 20 min at 160 °C in a compression press to obtain sheets that were 150 mm × 150 mm in area and approx. 2 mm in thickness.

Scanning electron microscopy (SEM) was used to analyze filler particles and cross-sections of the filled elastomers. Fractured surfaces of the elastomer specimens from the tensile testing experiments were cut and mounted on metal stubs by using conductive carbon tape. The samples were sputter-coated with a thin Au/Pd layer and imaged using a JEOL JSM 6300 field-emission scanning electron microscope. An accelerating voltage of 5 kV was used.

A Bruker D8 FOCUS diffractometer, equipped with a Ni foil filtered 0.154 nm Cu Kα line source (2.2 kW Cu anode), a Bragg-Brentano theta-2theta geometry, and a scintillation counter detector, was used to generate the X-ray diffraction (XRD) patterns of the fillers and the elastomer composites. Powder samples were used for the fillers, and bulk samples (≅ 2 mm thick discs of the elastomers) were used for the analysis of the composites. For data acquisition, the step width and dwell time were 0.1° and 8 s, respectively. The characterization was done at room temperature. A piecewise cubic Hermite interpolating polynomial was used for baseline subtraction in the reported patterns.

Dynamic mechanical analysis (DMA) was performed using a TA Instrument Q800 DMA instrument and an 8-mm dual cantilever clamp according to previously reported procedures [15]. Rectangular bar specimens of dimensions 20 × 13 × 2 mm^3 were punched out of the compression molded sheets. These specimens were annealed in a vacuum oven at 100 °C for 12 h before analysis. The frequency-sweep (*f*-sweep) DMA experiments were performed using an oscillatory strain of 0.1% strain amplitude, with the oscillation frequency increased logarithmically from 0.01 Hz to 10 Hz. The measurement temperature was about 30 °C. A Poisson's ratio of 0.44, a shear factor of 1.2 (accounting for the variation of shear strain across the bar cross-section), and the manufacturer-specified clamping factor were used for converting measured strain-amplitude and stiffness to strain and elastic modulus, respectively. The temperature-sweep (*T*-sweep) studies were carried out over a temperature range of − 150 °C to 200 °C at a constant heating rate of 3 °C min^{-1} with a strain amplitude of 0.1% and a frequency of 1 Hz.

Flat dumbbell-shaped tensile testing specimens with a gauge length of 20 mm and width of 2 mm were punched out of the elastomer sheets, and annealed at 100 °C for 12 h under vacuum. The tests were

Table 1
Elastomer composition.

	phr	wt %
HNBR	100	61.2
Filler	45	27.5
Peroxide vulcanizing agent (VUL-CUP 40 KE)	13.20	8.05[a]
N,N′-m-phenylene bismaleimide	0.90	0.55
4,4′-Bis(α,α-dimethylbenzyl)diphenylamine	2.60	1.60
Stearic acid	0.90	0.55
Zinc oxide	0.90	0.55

[a] 3.22 wt % active peroxide + 4.83 wt % clay.

conducted using a Universal Testing Machine (Instron 5900 R) with a 30 kN load cell controlled by a Bluehill 3 Testing Software (Instron). The crosshead movement was used for recording specimen elongation or displacement, Δ. Simple uniaxial tension tests were conducted under displacement control at an extension rate of 500 mm min^{-1}. Data reported herein are based on three replicate experiments for each material.

The dumbbell specimens were also subjected to cyclic tensile tests using a triangular strain waveform, consisting of loading and unloading of the specimen at a constant displacement rate of 50 mm min^{-1}. The amplitude of the engineering strain, in each set of 5 load-unload cycles, was increased in steps of 25% until the specimen fractured.

Fracture testing was performed using single edge notch tension (SENT) specimens, as discussed in Torabizadeh et al. [15]. Rectangular bar specimens of 100 mm length (50 mm length between grip ends), 15 mm width, and ≅ 2 mm thickness were punched from the elastomer sheets using a sharpened steel punch. They were annealed at 100 °C for 12 h under vacuum. A 2-mm edge notch was cut on one side, at the midpoint of the length of the specimen, using a sharp steel blade (nominal thickness of 0.23 mm). The crack length was then measured using a Nikon Eclipse L200 N microscope with a precision of 0.01 mm. Titanium dioxide was applied to the pre-cut notch surfaces to make the crack growth visible during the test. The elastomer filled with carbon fiber was cut parallel to the sheet rolling direction, so that the fibers were oriented, on an average, along the tensile axis of the specimen. The fracture tests were conducted using a Universal Testing Machine (Instron 5900 R) at room temperature. The extension rate was 5 mm min^{-1}. An AmScope MU300 digital camera was employed to capture images of the open notch and crack tip from a lateral view, at short time intervals during the test. Up to 50 images collected over a displacement range of 5–20 mm were analyzed to obtain the crack-tip-opening displacement (CTOD) vs. displacement, Δ, data. Experimental details on the calculation of CTOD are discussed in Torabizadeh et al. [15]. Strain energy, U, was obtained by integrating load, P, vs. displacement data, and used to calculate the strain energy release rate, $J^{sh} = U/B(W - a_0)$.. The material resistance to crack extension was characterized in terms of the resistance curve or R-curve, obtained by plotting J^{sh} vs. CTOD. The superscript "sh" denotes the fact that this formula for the strain energy release rate is based on a pure-shear tear specimen, for which the geometry factor is unity. Crack initiation resistance, J_{Ic}, and tear resistance, T_R, were obtained from the value of J^{sh} at crack initiation (CTOD ≅ 0.1 mm) and the slope of the R-curve at CTOD ≅ 0.2 mm, respectively, after applying a geometry factor correction pre-determined for SENT specimens [15].

3. Results and discussion

3.1. Elastomer composition

Elastomer compositions consisting of flat surface-functionalized clay nanoparticles (Nanomer I.31 PS) were compared with those incorporating agglomerates of conventional spherical carbon black nanoparticle (N550). Elastomers filled with flat graphite nanoparticles (Nano24) and elongated carbon fibers (AGM-94) were also included for comparison. Although not nanoscale in dimensions, the milled carbon fiber particles were used in the study to represent high aspect ratio fillers that are commonly used in polymer composites. The rubber compounds were prepared by mixing the filler with HNBR and other additives in an internal mixer and a two-roll mill. The molar compositions of butadiene, hydrogenated butadiene, and acrylonitrile units in HNBR were approx. 6.0 mol %, 56.5 mol %, and 37.5 mol %, respectively. Thus, the degree of unsaturation was relatively low, making hydrogen abstraction the primary mechanism for crosslinking. α,α′-Bis (*tert*-butylperoxy)-*m*/*p*-diisopropylbenzene (BBIPB), which produces high energy *tert*-butoxy and diisopropoxy radicals (capable of H abstraction) upon heating, was used for crosslinking the elastomer. BBIPB is relatively stable at temperatures below 100 °C, but exhibits a high radical production rate at the crosslinking temperature of 160 °C chosen in this study. At this temperature, the half-life of the first-order decomposition reaction in a non-reactive solvent, given by $\ln t_{1/2} = 18607.\ 7/T - 41.\ 05$ (where $t_{1/2}$ is the half-life in minutes and T is the absolute temperature) [16,17], is approx. 6.7 min. The half-life has been reported to be affected by the polymer in which the peroxide decomposes, and is generally higher in a solid polymer matrix than in a liquid solution obtained using an inert solvent. For example, the half-life of BBIPB in nitrile rubber is approx. 8.7 min at 160 °C [17].

A bifunctional monomeric coagent, *N,N′-m*-phenylene bismaleimide (*m*-PBM), was added to increase the degree of unsaturation (overall concentration of C=C bonds) in the elastomer formulation and obtain higher crosslinking. *m*-PBM is capable of grafting on the polymer backbone by a free-radical mechanism [18]. More importantly, it can react with nucleophilic functional groups present on the surface of the filler particles, for example, the $-NH_2$ groups of the surface-functionalized clay, by the aza-Michael addition reaction [19–21]. The aza-Michael reaction involves the addition of an amine to a conjugated unsaturated compound, for instance, an acrylate or a maleimide, to result in C–N bond formation [22]. Such a reaction, of an $-NH_2$ group on the clay particle surface with one of the maleimide groups of a *m*-PBM molecule, and a free radical grafting reaction of the other maleimide group of the same *m*-PBM molecule with HNBR, would lead to covalent attachment of the polymer chain to clay. Two amine-functionalized clay platelets can also be covalently linked by aza-Michael reactions with a given *m*-PBM molecule. The resulting formation of a crosslinked co-network of the elastomer and filler particles, as schematically depicted in Fig. 1, is expected to lead to an enhancement in the mechanical and fracture properties of the elastomers.

Table 1 gives the chemical composition of the crosslinked elastomer composites reported herein. A baseline elastomer prepared using the recipe given in Table 1 but without any of the four fillers of interest, was used for comparison. The focus of this article is on filled elastomers containing 45 parts of filler per hundred parts of polymer (denoted by 45 phr), a concentration that is significantly higher than the percolation threshold concentration of the particles [23]. To fully explore the property enhancement achieved by the surface-functionalized Mt clay, fracture properties are reported for elastomers containing two other concentrations of this clay (20 and 30 phr). A detailed correlation of mechanical properties to essential considerations such as filler volume fraction and surface area will be discussed in a separate report.

BBIPB was commercially available as a 40 wt % mixture with clay particles. Thus, all elastomers of the present study, including the baseline elastomer, contained about 8 phr (4.8 wt %) of organosilane-functionalized kaolin clay particles from the peroxide curing agent (see

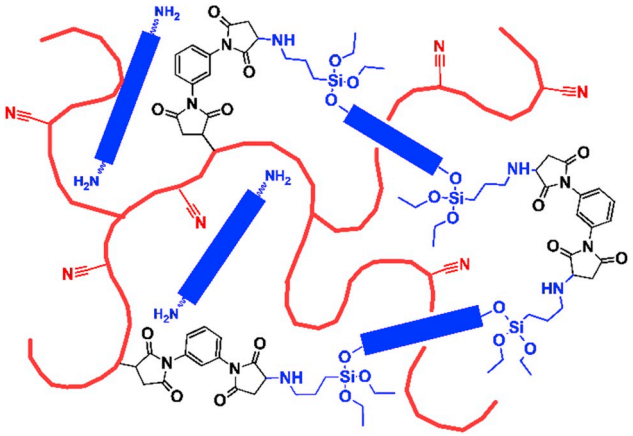

Fig. 1. Schematic of crosslinking of HNBR and amino-functionalized clay particles mediated by a peroxide and *N,N′-m*-phenylene bismaleimide coagent.

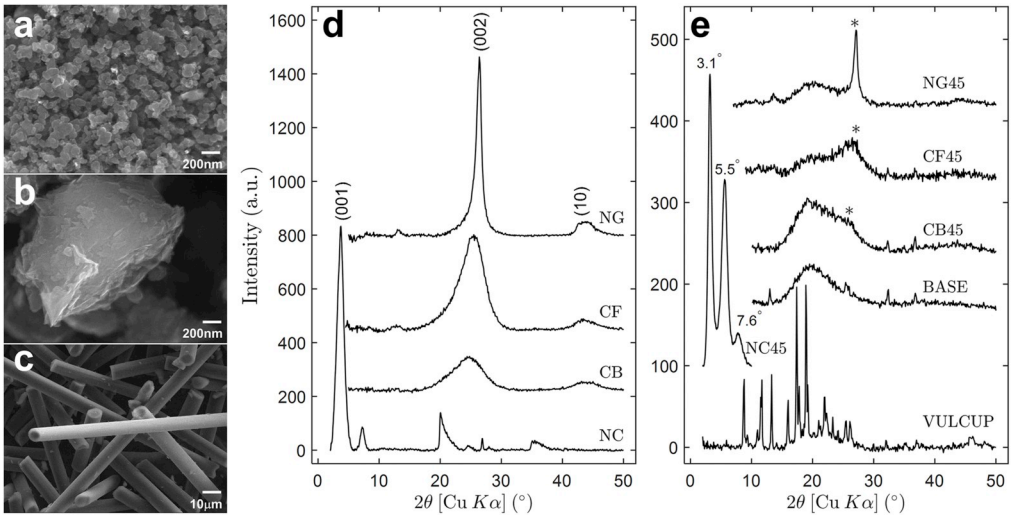

Fig. 2. SEM images of: (a) carbon black (CB); (b) nanographite (NG); and (c) carbon fiber (CF) particles. (d) Powder XRD patterns of NG, CF, CB, and surface-functionalized nanoclay (NC) particles. (e) XRD patterns of bulk specimens of NC45, NG45, CF45, CB45, and BASE; and powder XRD pattern of BBIPB peroxide curing agent loaded on organosilane-modified kaolin (Burgess KE) clay particles (VUL-CUP).

Table 1), in addition to the studied fillers. The elastomers incorporating particles of surface-functionalized nanoclay, nanographite, carbon black, and carbon fiber are denoted by NC45, NG45, CB45, and CF45, respectively. The baseline elastomer is denoted by BASE. Clay-filled elastomers with 20 and 30 phr concentrations of nanoclay are denoted by NC20 and NC30, respectively.

Fig. 2(a–c) shows SEM images of the as-received carbon black, graphite, and carbon fiber particles, along with their powder X-ray diffraction (XRD) patterns. The mechanically labile agglomerates of spherical carbon nanoparticles are seen in the SEM image of CB in Fig. 2(a). Fig. 2(b) shows a flat nanographite particle composed of layers of graphene sheets. The carbon fiber particles were much larger than either CB or NG. The milled polyacrylonitrile-based fiber particles had a carbon content of at least 94%, an average length of 150 μm, a fiber diameter of 7–9 μm [see Fig. 2(c)], and tensile strength in the range of 2.0–3.8 GPa (specified by the vendor).

The X-ray diffractogram of Nano24 graphite particles [Fig. 2(d)] showed a distinct (002) reflection that is characteristic of the interlayer spacing in graphite (which is 0.3354 nm in well-crystallized hexagonal graphite) [24,25]. A relatively broad diffraction profile that was difficult to resolve into separate sharp peaks was also observed over the 2θ range of 41°–45°, in the region where (10), (100) and (101) reflections are expected. The average number of graphene layers per graphite particle was estimated to be about 7.5, using the BET surface area of the nanographite particles and the theoretical surface area of graphene (2630 $m^2\ g^{-1}$). Compared with the Nano24 graphite particles, the carbon fiber and carbon black particles exhibited significantly broader asymmetric (002) and (10) peaks [see Fig. 2(d)], indicating the presence of turbostratic carbon in these fillers.

Fig. 2(d) also shows the XRD pattern of the Nanomer I.31 PS nanoclay, which is a Mt clay, modified by inner-gallery ion exchange with octadecyl ammonium cations [26–28] and edge-functionalized with γ-aminopropyltriethoxysilane (γ-APTES) [29]. The total concentration of these organic groups, determined by thermogravimetry, was about 30 wt % (see Fig. S1 in Supplementary Data).

Mt clay particles are made of $Al_2(Si_2O_5)_2(OH)_2$ platelets, approx. 1-nm thick, containing an octahedral sheet of aluminate sandwiched between two tetrahedral sheets of silicate [5]. The exchange of some of the Al^{3+} atoms with Mg^{2+} atoms imparts a negative charge to the platelets. Electroneutrality is obtained by the incorporation of cations such as Na^+ in the interlayer spaces (called the galleries) within the clay particle. In Nanomer I.31 PS, the adsorbed Na^+ cations were substituted by an ammonium cation with an extended organophilic group, which rendered the platelet surface less polar and more compatible with HNBR polymer.

Additionally, the hydroxyl groups present at the edges of the clay particles were reacted with the $–SiOCH_2CH_3$ segments of γ-APTES, resulting in pendant reactive amino groups [29]. Based on the information from the supplier, Nanomer I.31 PS contained up to 5 wt % of such particle-bound γ-APTES. The X-ray diffraction pattern in Fig. 2(d) shows a distinct (001) peak at 2θ equal to (3.7 ± 0.1)°, corresponding to a *d*-spacing of 2.4 ± 0.1 nm, attributed to reflections from the basal plane of the platelets. A second peak at (7.2 ± 0.1)° is also seen. This peak could correspond to the second-order reflection of the (001) planes (expected at $2\theta \cong 7.4 \pm 0.2°$) with the same *d*-spacing of 2.4 nm [30], or could also be a result of an interlayer spacing collapse discussed by other researchers [31]. A contraction of the *d*-spacing to a value of 1.2 nm could be because of side reactions between interlayer silane molecules leading to bridging and interlocking of the platelets, as hypothesized by Asgari et al. [29]. The intensity of the secondary peak was, however, relatively low (< 10% of the intensity of the peak at 3.7°) to warrant further detailed investigation in the present study. Other diffraction, peaks observed in the wide angle range of 20–40° are characteristic of Mt and quartz, as reported by Ahmed et al. [31].

The organophilic Mt and other clay minerals used in polymer nanocomposites are generally prepared either by the cation exchange reaction with a quaternary ammonium salt [26–28] or by silylation reaction with an organically modified alkoxysilane [29]. However, in the Nanomer I.31 PS particles of the present study, both ion exchange and silylation reactions were used to obtain surface-functionalized clay nanoparticles with dual functionality. The reactive hydroxyl groups required for the silylation reaction are located at the broken edges of the clay platelets [32], and the structural defects of the interlayer and external surfaces [33]. The edge hydroxyl groups are more accessible for the silylation reaction and are preferentially functionalized by γ-APTES [29,32].

Fig. 2(e) shows the XRD patterns of the baseline elastomer and the elastomer filled with carbon black, graphite, carbon fiber, and surface-functionalized clay. Compared with the diffraction patterns of the neat fillers, the diffraction intensities of the elastomer composites were weak. The XRD patterns in the case of BASE, CB45, and CF45 were dominated by diffraction peaks associated with kaolinite present in the VUL-CUP 40 KE initiator. However, all of the carbon-filled elastomers also showed the graphitic peak near 27° (indicated by an asterisk in the figure), which is expectedly quite prominent in the diffraction pattern of NG45.

The clay-filled elastomer showed multiple diffraction peaks, at approx. 3.1°, 5.5°, and 7.6°, corresponding to *d*-spacing of 2.8 nm, 1.6 nm, and 1.2 nm, respectively. If each of these diffraction peaks is assumed to originate from three different interlayer spacings, then a slight

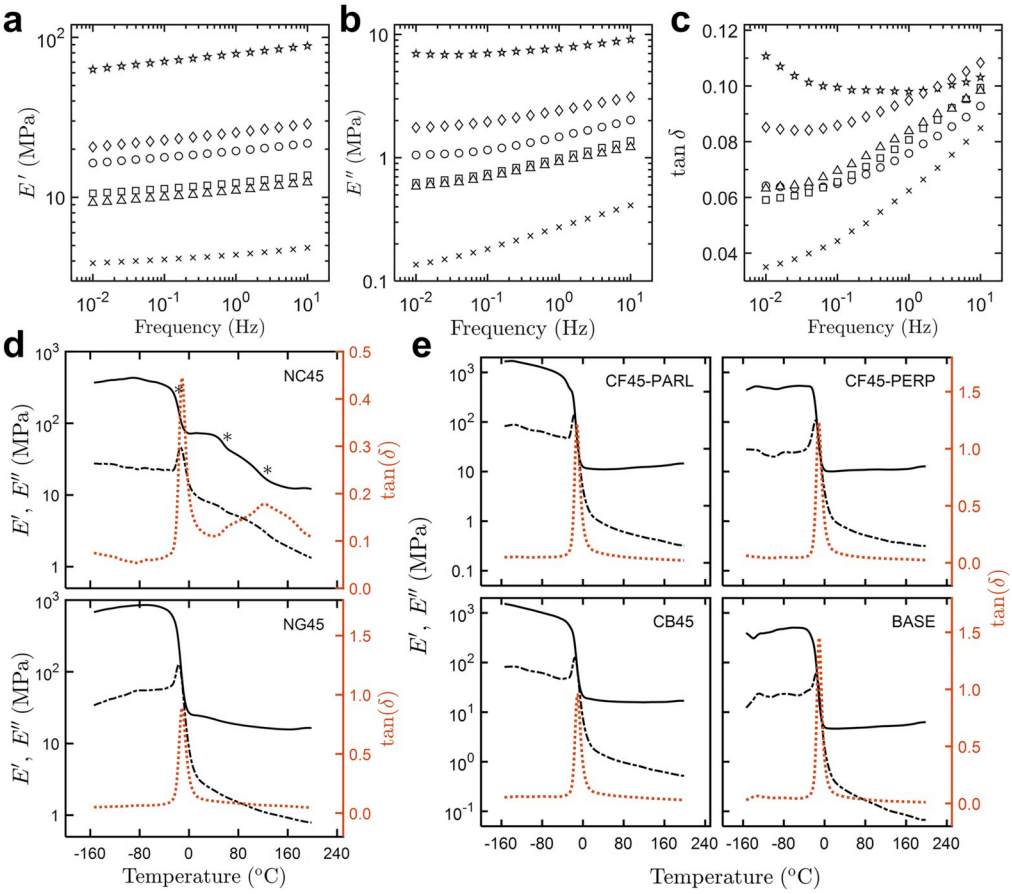

Fig. 3. (a–c) Frequency-sweep DMA results at 30 °C for NC45 (☆), NG45 (◇), CB45 (◯), CF45-PARL (□), CF45-PERP (△), and BASE (×). (d) Temperature-sweep DMA results for NC45 and NG45 elastomer composites showing E' (—), E'' (— · —), tan δ (·····), and the onset of glass transitions in NC45 (*). (e) Temperature-sweep DMA results for CF45-PARL, CF45-PERP, CB45, and BASE.

expansion from the initial value of 2.4 nm in some galleries, and a contraction to 1.6 nm and 1.2 nm in others, according to the mechanism of Asgari et al. [29] can be inferred.

The diffraction intensity was significantly lower in the case of NC45 than the clay powder. The lower diffraction intensity is obviously because of a lower concentration of the crystalline phase (the clay particles) in the bulk rubber specimen than in the neat filler. Only about 27.5 wt % of the elastomer composite is the surface-functionalized clay (see Table 1). The lower intensity could also be because of complete exfoliation of some of the clay particles into individual platelets during mixing with the elastomer in the internal mixer, followed by further shearing in the two-roll mill. In general, the XRD results show that a nanocomposite with well-dispersed filler particles, and molecular scale polymer–filler interactions, resulted from the compounding procedure.

3.2. Dynamic mechanical properties

3.2.1. Frequency sweep

Fig. 3(a – c) shows the storage and loss modulus, E' and E'', respectively, and loss tangent, $\tan\delta = E''/E'$, obtained from *f*-sweep DMA measurements on the elastomer specimens at different frequencies, at 30 °C. Table 2 gives these values at 1 Hz frequency. All of the filled elastomers exhibited higher modulus than BASE, as expected. Furthermore, E' of the elastomers containing the flat fillers, clay and graphite, were 4.0 × and 1.3 × higher, respectively, than CB45. The loss modulus was also higher for the flat fillers. The E'' values of NC45 and NG45 were 5.1 × and 1.6 × higher than CB45. Fig. 3(c) shows that tan δ was higher for NC45 and NG45, especially at the lower measurement frequencies, than CB45 or BASE. The carbon fiber filled elastomer, CF45, had a lower modulus [in both parallel and perpendicular orientations (*vide infra*)] than CB45. Its tan δ values were comparable to CB45.

Table 2
f-Sweep DMA results.[a]

	E' (MPa)	E'' (MPa)	tan δ
NC45	78.9	7.7	0.098
NG45	25.4	2.4	0.095
CB45	19.5	1.5	0.076
CF45-PARL	12.3	0.99	0.081
CF45-PERP	11.0	0.92	0.084
BASE	4.4	0.27	0.062

[a] Measurements at 30 °C in dual-cantilever mode at 1 Hz frequency and 0.1% strain amplitude.

CF45 exhibited anisotropy in mechanical properties, depending on whether the rectangular bar specimen was punched out from the pressed sheets, with length parallel to the direction of shear force in the two-roll mill (CF45-PARL) or perpendicular to this direction (CF45-PERP). The CF45-PARL specimen was stiffer than the CF45-PERP specimen, evidently because of the preferential alignment of the fibers along the direction of shear force in the roll mill. The differences between the CF45-PARL and CF45-PERP specimens were more pronounced in the tensile testing experiments discussed in section 3.3.

3.2.2. Temperature sweep

Fig. 3(d) and (e) show the *T*-sweep DMA results for the filled and baseline elastomer specimens. All specimens exhibited a primary glass transition over a temperature range of −26 °C to −3 °C, attributed to α-relaxation of the HNBR segments of the crosslinked elastomer. NC45 showed additional transitions at higher temperatures, indicating strong (covalent or physical) polymer – filler and filler – filler interactions. Three thermal transitions, with onset temperatures at 25 °C, 53 °C, and 119 °C, respectively, are seen in the log E' vs. T plot for NC45

Table 3
Glass transition temperatures and activation energy from DMA measurements.[a]

	T_g (°C)				$\log E'_G - \log E'_R$	area (K^{-1})	Q (kJ mol^{-1})
	E' onset	E' inflection	E'' peak	$\tan\delta$ peak			
NC45	-25.1(7)	-17.7(3)	-13.3	-12.5	0.649(5) [b]	0.0768(2)	254(1)
NG45	-22(1)	-14.5(6)	-16.4	-12.1	1.54(4)	0.190(1)	243(4)
CB45	-20.5(1)	-12.6(6)	-16.1	-11.8	1.62(3)	0.201(1)	242(3)
CF45-PARL	-20.5(8)	-14.0(4)	-17.2	-12.5	1.90(2)	0.260(1)	219(3)
CF45-PERP	-19.9(2)	-14.1(3)	-17.0	-12.5	1.743(4)	0.266(1)	197(1)
BASE	-22.4(5)	-14.4(4)	-14.9	-11.8	2.12(3)	0.294(1)	216(3)

[a] 3 °C/min heating rate, 0.1% strain amplitude, 1 Hz frequency
[b] the uncertainty in the least significant digit is given in parentheses; 0.649(5) means 0.649 ± 0.005

[Fig. 3(d)]. The transition at 53 °C is close to the order-disorder transition of octadecyl ammonium surfactant present in the clay [28,34,35], and perhaps related to the melting of inner-gallery smectic bilayers of the surfactant molecules. The transition at 119 °C can be attributed to polymer layers of reduced mobility surrounding the clay particles as hypothesized by other researchers [23,34]. In fact, Fukahori's theory of stress softening of filled elastomers (cf. section 3.3.2) is based on buckling of stretch-oriented molecular bundles connecting these glassy layers [36]. However, similar multiple transitions were absent in the DMA thermograms of CB45, CF45, and even NG45 containing flat graphite particles. Thus, the glass transition at 119 °C is more likely due to microdomains formed by covalent linking of clay particles with the polymer matrix, as depicted in Fig. 1.

Table 3 gives the characteristics of the primary transition, in terms of the temperatures corresponding to the onset and inflection points in the $\log E'$ vs. T plot, and the E'' and $\tan\delta$ maxima. The primary glass transition temperature (T_g) was not strongly affected by the presence of the filler. The clay particles, however, showed a weak plasticization effect in that the E' onset and inflection temperatures were about 3 °C lower than the baseline elastomer.

Sadhu and Bhowmick found that the $\tan\delta$ peak height decreased and the position of the $\tan\delta$ peak changed marginally (by 1 or 2 °C) with the addition of a small amount (4 phr) of octadecyl amine modified and unmodified montmorillonite clays to SBR and nitrile butadiene rubber (NBR) [37]. The results shown in Fig. 3 and Table 3, for the elastomer composites of the present study, are consistent with their report. The peak height (or area) is related to the activation energy of glass transition, as discussed in the following section.

3.2.3. The activation energy of glass transition

In the dynamic mechanical analysis of a Maxwell material with single relaxation time, τ, the loss modulus, E'', is related to frequency, ω, by:

$$E'' = \frac{(E_\infty - E_0)\omega\tau}{1 + \omega^2\tau^2} \tag{1}$$

If the time constant, τ, shows an Arrhenius dependence on temperature, $\tau = \tau_0 \exp(Q/RT)$ where Q is the activation energy that is independent of temperature, Read and Williams [38] have shown that

$$Q = \frac{(E_\infty - E_0)\pi R}{2\int_0^\infty E''\mathrm{d}\left(1/T\right)} \tag{2}$$

where E_∞ and E_0 are the high and low frequency modulus, respectively, R is the gas constant, and T is the absolute temperature. Eq. (2) has been shown valid for materials with a distribution of relaxation times, described by empirical equations such as Fuoss-Kirkwood, Cole-Cole, and Cole-Davidson, or even a completely general distribution of relaxation times for which the average activation energy is $\langle 1/Q\rangle_{av}^{-1}$ [38]. The activation energy is proportional to the strength of the transition, given by the modulus difference, $E_0 - E_\infty$, and inversely proportional to the area under the E'' vs. $1/T$ curve. Using Eq. (2) as the basis, Sperling and co-workers [39] proposed the following equations for estimating Q from the area under the loss tangent curve:

$$Q = \frac{-(\ln E'_G - \ln E'_R)\pi R}{2\int_{T_G}^{T_R} \tan\delta\ \mathrm{d}\left(1/T\right)} \tag{3a}$$

$$\cong \frac{(\ln E'_G - \ln E'_R)\pi R T_g^2}{2\int_{T_G}^{T_R} \tan\delta\ \mathrm{d}T} \tag{3b}$$

In Eq. (3), the strength of the transition is given by the difference in the logarithms of the storage modulus values in the glassy and rubbery states, and T_G and T_R are glassy and rubbery temperatures, just below and just above the glass transition temperature, respectively.

Table 3 gives the values of the activation energy for the predominant $\tan\delta$ peaks observed in Fig. 3(d) and (e). The area under $\tan\delta$ vs. $1/T$ was used to calculate Q using Eq. (3a). Illustrative calculations are shown for CB45 and NC45 in Supplementary Data (Figs. S2 and S3). It is seen that the activation energy is significantly higher for NC45, NG45, and CB45 compared with the baseline elastomer. It is the highest for NC45. The higher activation energy is an evidence for polymer–filler interfacial interactions at the molecular level. Note that these interactions do not reflect in an increase in T_g. The observed T_g of NC45, corresponding to this transition, is in fact lower than that of the baseline elastomer. The activation energy of CF45-PERP is unexpectedly low, but is consistent with the relatively low elongation at break, crack initiation resistance, tear resistance, and other properties discussed in sections 3.3 and 3.4.

3.3. Tensile testing

3.3.1. Linear extension until fracture

Fig. 4 shows representative stress vs. strain curves of the elastomers in the present study. All the filled elastomers exhibited higher initial elastic modulus (slope of stress vs. strain) compared with BASE (see Table 4). The clay-filled elastomer stands out as having not only a higher stiffness than CB45 or NG45, but also higher ductility (elongation at break) and modulus of toughness (area under stress − strain plot until fracture).

In the case of CF45-PARL, the particles of carbon fiber are preferentially oriented along the stretch direction. Fig. 4(a) clearly shows that this elastomer is significantly stiffer than CF45-PERP in which the fibers are oriented perpendicular to the stretch direction (consistent with the observations of Mortazavian and Fatemi [40], who studied tensile properties of short fiber reinforced composites consisting of glass fibers and thermoplastic polymers). Of the different elastomers compared in Table 4, NC45 and NG45 that contained flat filler particles were found to have a higher elongation at break and a higher modulus of toughness than CB45. NC45 was about two times tougher than CB45.

The tensile properties of HNBR elastomers incorporating Mt clay particles of the present study, modified with both octadecyl ammonium and aminopropyl groups, are observed to be better than elastomers

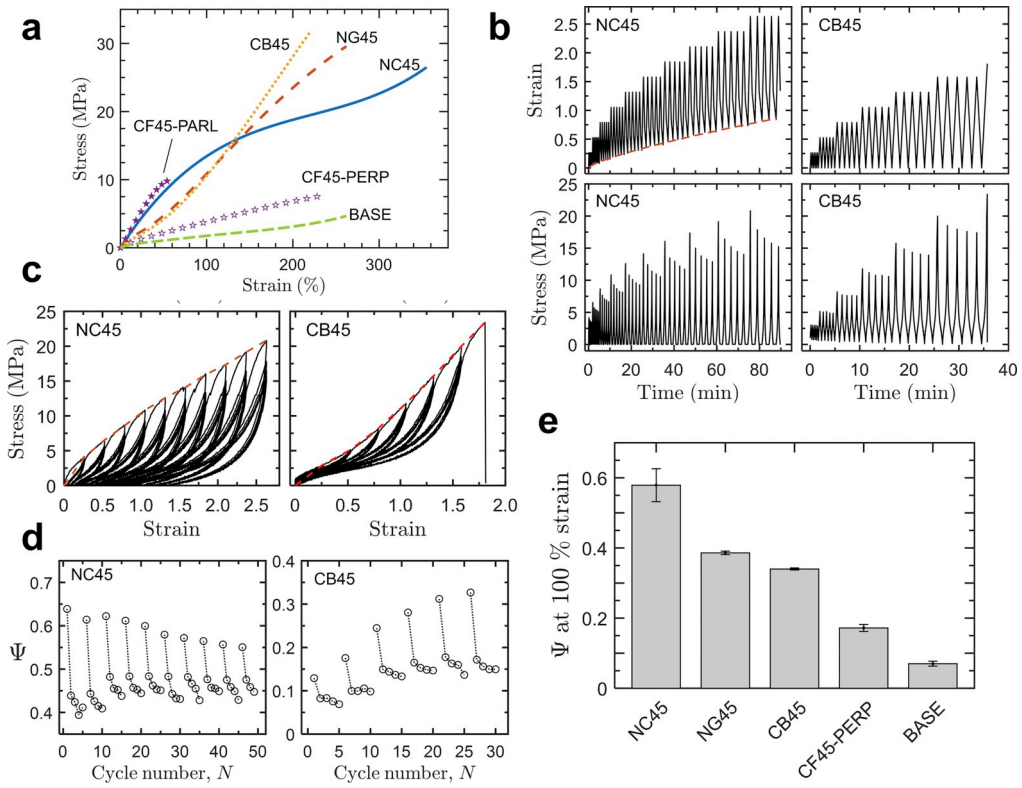

Fig. 4. (a) Stress vs. strain results at room temperature acquired at 500 mm min^{-1} extension rate. (b) Strain vs. time and stress vs. time plots for NC45 and CB45 during cyclic testing at a displacement rate of 50 mm min^{-1}. (c) Stress vs. strain plots for NC45 and CB45 during cyclic testing. (d) Dissipated energy fraction vs. cycle number for NC45 and CB45. (e) Dissipated energy fraction at 100% strain (cycle # 16) for all elastomer composites. CF45-PARL is not shown because sample fractured before 100% strain. All data were acquired at room temperature.

Table 4
Tensile properties of un-notched dumbbell specimens.[a]

	Initial elastic modulus (MPa)	Ultimate tensile strength (MPa)	Elongation at break (%)	Modulus of toughness (MPa)
NC45	16(2)	24(2)	330(20)	53(8)
NG45	11(1)	28(2)	250(10)	35(4)
CB45	7.6(4)	28(5)	205(20)	25(7)
CF45-PARL	22.5(2)	9.9(5)	63(1)	3.9(2)
CF45-PERP	3.6(5)	8.1(5)	255(8)	12(1)
BASE	1.7(4)	3.9(6)	235(30)	5(1)

[a] The uncertainty in the least significant digit is given in parentheses; it is estimated from standard deviation of three measurements.

containing clay particles modified with octadecyl ammonium groups alone. The tensile strength and elongation at break reported by Zhang et al. [41] for an optimal composition of the latter system (identified to be 10 phr of octadecyl ammonium functionalized Mt clay) are 9.61 MPa and 268%, respectively. In contrast, the corresponding values for NC45 are significantly higher (24 MPa and 330%, respectively), attributed to the reactivity of the aminated clay particles with *m*-PBM.

3.3.2. Cyclic tensile testing and strain energy dissipation

Fig. 4(b–d) show results from cyclic tensile testing conducted to characterize stress softening, hysteresis, and strain energy dissipation in the elastomers of the present study. The results shown are for CB45 and NC45, but measurements were conducted for all the elastomers, with two replicates for each material. The results for NG45, CF45-PARL, CF45-PERP, and BASE are given in Supplementary Data (Fig. S4 − S7).

The experiments were conducted in the displacement-control mode, wherein the stress response to an applied strain variation is measured. Fig. 4(b) shows the cyclic strain profile used. The values reported are of the engineering strain. The specimen was subjected to each strain level for five cycles, and the strain level was increased in increments of 25% until the specimen fractured. The lower bound of the strain profile, indicated by a dashed curve in Fig. 4(b) (in the panel for NC45) is because of the creep phenomenon, as elaborated below.

The stress response, calculated from the force values recorded by the load cell and the original cross-sectional area of the gauge section of the specimen, is also shown in Fig. 4(b) (bottom panels). It is evident that, at each strain level, the stress required to attain the strain decreased from one cycle to the next. This effect, reported as early as 1903 [42], and comprehensively reviewed by Mullins [43], is referred to as stress softening, or the Mullins effect. Although general agreement on the physical origin of the Mullins effect has not been reached [44], it likely has contributions from the rupture of filler agglomerates [45,46], release of trapped entanglements [47,48], buckling of stretch-oriented molecular bundles connecting the surfaces of filler particles [36], and dissipative friction due to internal sliding of the polymer chains and sliding of the chains at the surface of the reinforcing filler particles [49]. The stress vs. strain plot in Fig. 4(c) shows the mechanical hysteresis that results because of the stress-softening effect. In each loading-unloading cycle, the stress required during loading, to achieve the stipulated strain vs. time profile, is higher than the stress required when the specimen is unloaded (that is, allowed to recover to the original unstressed state). The upper envelope of the experimentally measured hysteresis loops, such as the dashed stress vs. strain curve in Fig. 4(c), was generally found to be in good agreement with the stress vs. strain curve obtained in a linear (non-cyclic) extension of a pristine specimen at the same displacement rate.

The area below the stress vs. strain curve during loading is the energy expended per unit volume of the specimen during extension, and the area below the stress vs. strain curve during unloading is the

recovered energy. The recovered energy is lower than the expended energy, and the difference is attributed to viscous dissipation within the material.

Fig. 4(d) shows the dissipated energy fraction, Ψ, also called the plasticity index, (see Sreeram et al. [50] for a schematic of its calculation using the dissipated and recovered energies), for each of the loading-unloading measurements conducted on NC45 and CB45. The clay-filled elastomer could be extended to a strain of 250% (50 cycles), in contrast with CB45 that fractured at 175% strain (31 cycles). It is seen that Ψ is the highest during the first of the five cycles of a given strain range. The Ψ values of NC45 are significantly higher than that of CB45, and they show a somewhat weaker cycle-to-cycle variation. For NC45, Ψ decreased in the range of 0.64 to 0.55 over 46 cycles, whereas, for CB45, Ψ increased from 0.13 to 0.33 over 26 cycles.

Fig. 4(e) gives a comparison of the values of Ψ for the different elastomers. A strain range of 0–100% (cycle # 16) was used for this comparison. Ψ values for all cycles are given in Fig. S8 of Supplementary Data. The baseline elastomer showed the lowest Ψ, which is consistent with the fact that the polymer − filler interfacial forces are the weakest in BASE because of minimal filler concentration in this material (coming exclusively from the VUL-CUP 40 KE vulcanizing agent). Correspondingly, the highest value of Ψ observed in the case of NC45 leads to the inference that polymer − filler interfacial interactions are the strongest in the clay-filled elastomer. Furthermore, for a given filler volume, flat filler particles would have a higher surface area than spherical nanoparticles, which explains the higher Ψ of NG45 compared with CB45. The observed variation of Ψ with filler type agrees well with the variation in fracture properties presented in section 3.4.

The clay-filled elastomer exhibited significant creep during cyclic tensile testing. As seen in Fig. 4(b), a permanent deformation (extension) was observed at the end of each cycle. Because of this permanent deformation, the strain did not recover to a value of 0 when the stretched specimen was unloaded to the unstressed state (applied stress = 0). The dashed curve in Fig. 4(b), in the strain vs. time plot for NC45 (top left panel), corresponds to the increase in the length of the specimen with time because of permanent deformation under tensile load. Because of an increase in the gauge length of the specimen, compressive stress was necessary to force the crosshead displacement to its initial value of 0 (that is to make the engineering strain equal to 0). These negative stress values, which are not related to the strain energy of the material (but only cause buckling of the elongated specimen), were accordingly excluded during the determination of all values of Ψ reported herein.

3.4. Fracture properties

3.4.1. Crack initiation and propagation resistance

The results of uniaxial quasi-static fracture tests on single edge notch tensile (SENT) specimens [15], with approx. 2 mm edge notch, are shown in Fig. 5 and Table 5. A discussion of the theoretical basis for fracture analysis can be found in Ref. [15]. In Fig. 5(a), the tensile stress, based on the surface area of the initial uncracked ligament $[=B(W-a_0)]$, is plotted against displacement. P is the applied load, B is the specimen thickness (≅2 mm), W is the specimen width (≅15 mm), and a_0 is the initial crack length (≅2 mm). Fig. 5(b) shows the crack resistance curves, or R-curves [15], of the elastomers. The strain energy, U, was calculated by integrating the P vs. Δ curve, up to the displacement, Δ, corresponding to a given experimentally measured CTOD. A qualitative comparison of the R-curves indicates that the strongest enhancement of fracture resistance is provided by the flat fillers, clay and graphite. Both NC45 and NG45 exhibited significantly higher strain energy than CB45 [Fig. 5(b)], and not surprisingly, the baseline elastomer. The CF45-PARL specimen that showed high stiffness in tensile testing of the un-notched specimen exhibited very poor fracture properties. Its R-curve was below that of even CF45-PERP.

Table 5 gives the values of the critical J-integral for mode I loading, J_{Ic}, which is a measure of the resistance of a material to crack initiation. J_{Ic} was obtained from the R-curve [Fig. 5(b)] using ordinate values corresponding to CTOD = 0.1 mm and applying the geometry factor correction ($\eta = 0.6$) [15]. The tear resistance, T_R, was similarly obtained from the product of the geometry factor and the slope of the R-curve at CTOD = 0.2 mm.

The crack initiation resistance of the clay-filled NC45 elastomer was about two times that of the elastomer filled with carbon black (CB45), and approximately five times that of the baseline elastomer. The graphite-filled NG45 has approximately the same crack initiation resistance as CB45, but a significantly higher tear resistance (more than 2× that of CB45). The tear resistance of NC45 is 6× that of CB45, which is disproportionately higher compared with the approx. 2× enhancement in toughness (cf. section 3.3.1).

The improvement in fracture properties is attributed to the better ability of a clay or graphite particle to arrest crack growth at the microscale, because of a stiff physical barrier generated by their 2-D surface, when the surface is aligned orthogonal to the direction of crack-tip propagation. They are also able to dissipate strain energy in the form of viscous dissipation better (as shown in section 3.3.2), instead of directing the strain energy toward an increase in crack surface energy and surface area.

The significantly higher fracture resistance of the elastomer filled with surface-functionalized clay compared with CB45, and even NG45 containing flat filler particles, is attributed to the m-PBM mediated reaction of the filler particles with the polymer matrix (see Fig. 1). The filler concentration in NC45 is sufficiently high so that the particles are in close vicinity of each other and interparticle covalent bonding is also possible. Indeed, lower filler concentrations of 2-D fillers, such as those in the 4-phr (1.6 vol %) graphene-oxide/natural-rubber nanocomposites evaluated by Dong et al. [11] do not show fracture resistance enhancement. Carbon-based filler particles may also contain reactive surface functional groups such as hydroxyl [51], but their concentration and reactivity with m-PBM would be significantly lower than those of the specifically aminated clay particles used herein.

The surface-functionalized clay particles of the present study are highly effective in that elastomer composites incorporating these had significantly higher tear resistance than CB45 even at a lower clay concentration of 30 or 20 phr (see data for NC30 and NC20 in Table 5). Contrary to the observations of Nadiv et al. [9], a monotonic increase in fracture properties was observed in the filler concentration range of 20–45 phr, for the nanocomposite compositions reported herein.

The incorporation of carbon fiber improved the crack initiation resistance compared with the baseline elastomer, but J_{Ic} of CF45 was lower than that of CB45, in both parallel and perpendicular orientations. Interestingly, the carbon fibers result in a relatively high value of tear resistance if the fibers are oriented perpendicular to the stretch direction. T_R of CF45-PERP was about 1.5× that of CB45.

3.4.2. Analysis of fractured surfaces

The differences in the fracture behaviors of the elastomers containing the different types of fillers are evident from the SEM images of the fractured surfaces shown in Fig. 5(c–h). The rough fractured surfaces of NC45 and NG45, with a higher interfacial area, point to the higher energy expended in creating these surfaces, and consequently, higher resistance to crack propagation. In contrast, the fractured surface of CB45 [Fig. 5(g)] was smoother, which indicates weaker cohesive forces within the material.

Fig. 5(e) and (f) show the fractured surfaces of CF45-PARL and CF45-PERP, respectively. Higher magnification of the CF45-PARL surface is shown in Fig. 5(h). An adhesive failure, due to the weak polymer − filler bonding in the CF45 elastomer and the resulting fiber pull-off is quite evident. From these images, the polymer − filler interface may seem more vulnerable to crack propagation.

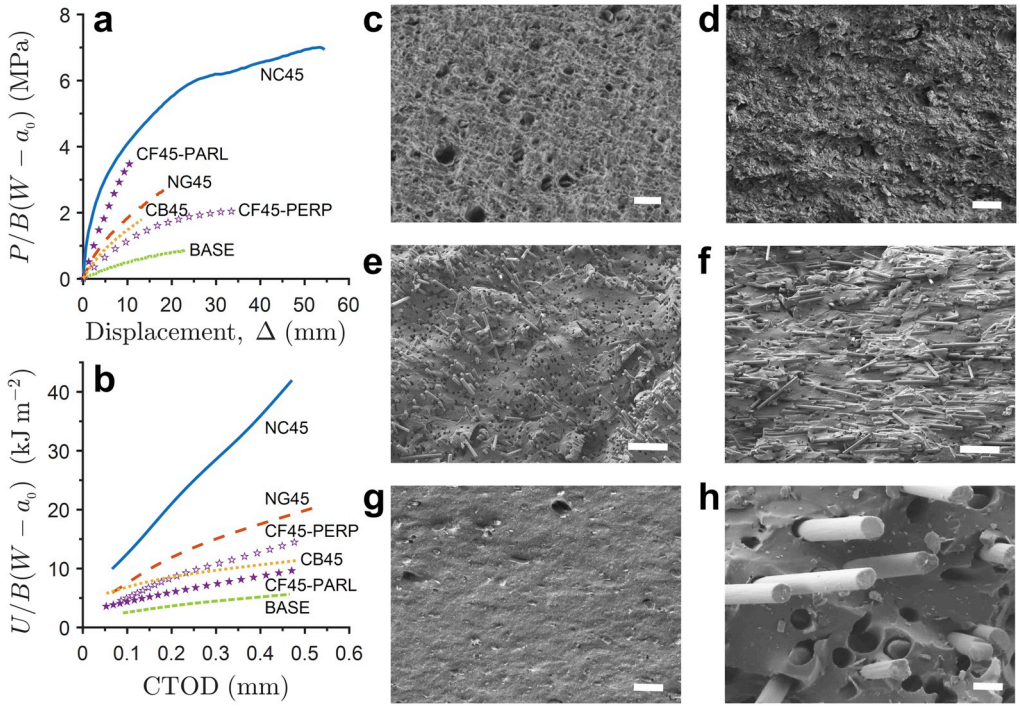

Fig. 5. (a) Load, P, (normalized by the initial area of the uncracked ligament) vs. displacement, Δ, measured during fracture testing of single edge notch tension (SENT) rubber specimens of thickness, B, width, W, and initial crack length, a_0. (b) R-curves: strain energy (normalized by area of the uncracked ligament) vs. crack-tip-opening displacement (CTOD). SEM images of fractured surfaces of: (c) NC45; (d) NG45; (e, h) CF45-PARL; (f) CF45-PERP; and (g) CB45. Scale bars correspond to 10 μm in all images except (e) and (f) where they represent 100 μm.

Table 5
Critical J-integral and tearing modulus at room temperature.[a]

	J_{Ic} (kJ m^{-2})	T_R (MPa)
NC45	7.5(9)	49(2)
NC30	6(1)	29(3)
NC20	3.5(5)	10.5(6)
NG45	5.6(4)	22(1)
CB45	4.2(4)	8(3)
CF45-PARL	2.7(4)	8(3)
CF45-PERP	2.9(4)	13(3)
BASE	1.5(2)	4(1)

[a] The uncertainty in the least significant digit is given in parentheses; it is estimated from the standard deviation of up to three measurements.

However, as discussed in section 3.4.1, the crack propagation resistance of CF45 was higher when the fibers were oriented along the direction of crack propagation, as seen in Fig. 5(f). The fibers in this SEM image of the fractured surface of CF45-PERP are seen lying parallel to the fractured surface. (Contrast this with the fractured surface of CF45-PARL shown in Fig. 5(e), in which the fibers are seen pointing out of the fractured surface.)

A crack propagating in CF45-PERP has to encounter a thicker high-stiffness barrier (namely, the carbon fiber), whose dimension scales with the length of the fiber. Crack advancement would require breakage of polymer−fiber interfacial forces throughout the length of the fiber. In contrast, a crack that is advancing in CF45-PARL encounters a thinner barrier, whose maximum thickness scales with the fiber radius (≅2×radius), which is significantly smaller than the fiber length, because of the high aspect ratio of the fiber particles. The interfacial forces that have to be overcome for crack propagation are corresponding smaller (corresponding to an interface length of $\pi \times$ fiber radius). Hence, crack propagation in CF45-PARL would require less energy, consistent with the R-curves shown in Fig. 5(b).

4. Conclusion

Remarkable enhancement in the mechanical and fracture properties of HNBR elastomer nanocomposites was observed due to the incorporation of flat filler particles (aspect ratio > 1) compared with spherical carbon black particles (aspect ratio = 1) or elongated carbon fiber particles (high aspect ratio ≫ 1). Nanoclay and nanographite fillers resulted in significant improvements in stiffness, ductility, and toughness of the elastomer. Compared with carbon black, about 100% enhancement in stiffness and toughness was obtained because of the clay nanoparticles, and up to 45% increase in the corresponding properties was observed in the case of graphite. The clay particles also imparted more than 500% improvement in tear resistance compared with carbon black. The graphite particles produced a 100% increase, in comparison.

Such unexpectedly high improvements, especially in the fracture properties, resulting from the incorporation of a clay filler is attributed to the synergistic effect of: (1) the physical barrier imposed by the flat (predominantly 2-D) filler particles to an advancing crack tip; and (2) the improved ability to release strain energy in the form of non-damaging viscous dissipation. The dissipated energy fraction was the highest for the clay-filled elastomer because of higher interfacial area per unit volume (related to the particle's flat aspect ratio) and strong polymer−filler and filler−filler interactions (because of interfacial bonding).

Surface functionalization of the Mt clay nanoparticles is critical in improving interfacial interactions of clay platelets that are intrinsically polar and poorly miscible with the polymer matrix. The lateral surfaces and edges of the Mt clay particles were functionalized with octadecyl groups and propyl amine groups, respectively. The nonpolar octadecyl groups promoted miscibility and dispersion of the clay platelets with the nonpolar polybutadiene domains of the polymer matrix. The reactive amino groups allowed covalent interlinking of the polymer−filler and filler−filler surfaces, utilizing the *N,N′-m*-phenylene bismaleimide coagent. The clay-filled elastomer exhibited multiple

glass transition in dynamic mechanical analysis, indicative of micro-domains comprising of these polymer – filler and filler – filler bonds, with different relaxation times. Some of the unusual and generally incompatible properties found for the clay-filled elastomer of this study—such as lower T_g but higher storage and loss moduli, higher ductility but higher stiffness, and higher elastic storage modulus but also higher viscous dissipation ($\tan\delta$ and Ψ)-can be associated with the formation of a polymer – filler co-network. It is expected that the novel materials reported here, with highly promising mechanical and fracture properties, will be useful in various applications where tougher and stronger elastomers are required.

Data availability

The data required to reproduce these findings are available to download from the Mendeley Data repository (https://doi.org/10.17632/d2hvcm3f7j.1).

Acknowledgments

Financial support from GE Oil & Gas and the Clarkson University Center for Advanced Materials Processing is gratefully acknowledged.

Appendix A. Supplementary data

Supplementary data to this article can be found online at https://doi.org/10.1016/j.polymertesting.2019.105932. These include thermogravimetric analysis of surface-functionalized clay nanoparticles, calculation of activation energy of glass transition, cyclic tensile testing results for NG45, CF45, and BASE elastomers, and dissipated energy fraction vs. cycle number.

References

[1] A.K. Zachariah, A.K. Chandra, P.K. Mohammed, S. Thomas, Vulcanization kinetics and mechanical properties of organically modified nanoclay incorporated natural and chlorobutyl rubber nanocomposites, Polym. Test. 76 (2019) 154–165.
[2] B. Mensah, K.C. Gupta, G. Kang, H. Lee, C. Nah, A comparative study on vulcanization behavior of acrylonitrile-butadiene rubber reinforced with graphene oxide and reduced graphene oxide as fillers, Polym. Test. 76 (2019) 127–137.
[3] J. Lin, S.H. Bang, M.H. Malakooti, H.A. Sodano, Isolation of aramid nanofibers for high strength and toughness polymer nanocomposites, ACS Appl. Mater. Interfaces 9 (2017) 11167–11175.
[4] J.S. Vélez, S. Velásquez, D. Giraldo, Mechanical and rheometric properties of gilsonite/carbon black/natural rubber compounds cured using conventional and efficient vulcanization systems, Polym. Test. 56 (2016) 1–9.
[5] D.R. Paul, L.M. Robeson, Polymer nanotechnology: nanocomposites, Polymer 49 (2008) 3187–3204.
[6] S.-Y. Fu, X.-Q. Feng, B. Lauke, Y.-W. Mai, Effects of particle size, particle/matrix interface adhesion and particle loading on mechanical properties of particulate–-polymer composites, Compos. B Eng. 39 (2008) 933–961.
[7] M. Maiti, M. Bhattacharya, A.K. Bhowmick, Elastomer nanocomposites, Rubber Chem. Technol. 81 (2008) 384–469.
[8] G. Kraus, Reinforcement of elastomers by carbon black, Angew Makromol. Chem. 60 (1977) 215–248.
[9] R. Nadiv, G. Shachar, S. Peretz-Damari, M. Varenik, I. Levy, M. Buzaglo, E. Ruse, O. Regev, Performance of nano-carbon loaded polymer composites: dimensionality matters, Carbon 126 (2018) 410–418.
[10] B. Zhong, Z. Jia, Y. Luo, D. Jia, F. Liu, Understanding the effect of filler shape induced immobilized rubber on the interfacial and mechanical strength of rubber composites, Polym. Test. 58 (2017) 31–39.
[11] B. Dong, L. Zhang, Y. Wu, Influences of different dimensional carbon-based nanofillers on fracture and fatigue resistance of natural rubber composites, Polym. Test. 63 (2017) 281–288.
[12] M. Sankarasubramanian, Filler Shape and Surface Chemistry Effects on Compressive Strength, Energy Dissipation, and Elastic Recovery of HNBR Elastomer Nanocomposites, Ph.D. Dissertation Clarkson University, Potsdam, New York, 2016.
[13] K.K. Sadasivuni, Y. Grohens, Nonlinear viscoelasticity of two dimensional filler reinforced rubber nanocomposites, in: D. Ponnamma, S. Thomas (Eds.), Non-Linear Viscoelasticity of Rubber Composites and Nanocomposites: Influence of Filler Geometry and Size in Different Length Scales, Springer International Publishing, Cham, 2014, pp. 43–57.
[14] R. Scotti, L. Conzatti, M. D'Arienzo, B. Di Credico, L. Giannini, T. Hanel, P. Stagnaro, A. Susanna, L. Tadiello, F. Morazzoni, Shape controlled spherical (0D) and rod-like (1D) silica nanoparticles in silica/styrene butadiene rubber nanocomposites: role of the particle morphology on the filler reinforcing effect, Polymer 55 (2014) 1497–1506.
[15] M. Torabizadeh, Z.A. Putnam, M. Sankarasubramanian, J.C. Moosbrugger, S. Krishnan, The effects of initial crack length on fracture characterization of rubbers using the *J*-Integral approach, Polym. Test. 73 (2019) 327–337.
[16] L.H. Palys, Peroxide cure systems, in: J.S. Dick (Ed.), Rubber Technology: Compounding and Testing for Performance, 2nd ed., Hanser Publications, Cincinnati, OH, 2009, pp. 411–437.
[17] Technical Information: VUL-CUP® Peroxide, Bulletin ORC-301M, Arkema Inc., Philadelphia, PA, 2009.
[18] T. Inoue, Selective crosslinking in polymer blends. I. Novel selective crosslink systems for polypropylene/unsaturated elastomer blends, J. Appl. Polym. Sci. 54 (1994) 709–721.
[19] I.K. Varma, S. Sharma, Curing of bismaleimides—I. Effect of amines on the curing behaviour and thermal stability, Eur. Polym. J. 20 (1984) 1101–1105.
[20] D.P. Fasce, R.J.J. Williams, Polycondensation of bismaleimides with aromatic diamines, Polym. Bull. 34 (1995) 515–522.
[21] D.B. Curliss, B.A. Cowans, J.M. Caruthers, Cure reaction pathways of bismaleimide polymers: a solid-state ^{15}N NMR investigation, Macromolecules 31 (1998) 6776–6782.
[22] G.B. Desmet, D.R. D'hooge, P.S. Omurtag, P. Espeel, G.B. Marin, F.E. Du Prez, M.-F. Reyniers, Quantitative first-principles kinetic modeling of the aza-Michael addition to acrylates in polar aprotic solvents, J. Org. Chem. 81 (2016) 12291–12302.
[23] G. Ramorino, F. Bignotti, S. Pandini, T. Riccò, Mechanical reinforcement in natural rubber/organoclay nanocomposites, Compos. Sci. Technol. 69 (2009) 1206–1211.
[24] N. Iwashita, Chapter 2 - X-ray powder diffraction, in: M. Inagaki, F. Kang (Eds.), Materials Science and Engineering of Carbon, Butterworth-Heinemann, 2016, pp. 7–25.
[25] Z.Q. Li, C.J. Lu, Z.P. Xia, Y. Zhou, Z. Luo, X-ray diffraction patterns of graphite and turbostratic carbon, Carbon 45 (2007) 1686–1695.
[26] M. Balachandran, S.S. Bhagawan, R. Muraleekrishnan, Modeling and optimizing properties of nanoclay–nitrile rubber composites using Box–Behnken design, Rubber Chem. Technol. 84 (2011) 455–473.
[27] H. Heinz, R.A. Vaia, R. Krishnamoorti, B.L. Farmer, Self-assembly of alkylammonium chains on montmorillonite: effect of chain length, head group structure, and cation exchange capacity, Chem. Mater. 19 (2007) 59–68.
[28] M.A. Osman, M. Ploetze, P. Skrabal, Structure and properties of alkylammonium monolayers self-assembled on montmorillonite platelets, J. Phys. Chem. B 108 (2004) 2580–2588.
[29] M. Asgari, A. Abouelmagd, U. Sundararaj, Silane functionalization of sodium montmorillonite nanoclay and its effect on rheological and mechanical properties of HDPE/clay nanocomposites, Appl. Clay Sci. 146 (2017) 439–448.
[30] K.G. Gatos, L. Százdi, B. Pukánszky, J. Karger-Kocsis, Controlling the deintercalation in hydrogenated nitrile rubber (HNBR)/organo-montmorillonite nanocomposites by curing with peroxide, Macromol. Rapid Commun. 26 (2005) 915–919.
[31] A. Ahmed, Y. Chaker, E.H. Belarbi, O. Abbas, J.N. Chotard, H.B. Abassi, A.N. Van Nhien, M. El Hadri, S. Bresson, XRD and ATR/FTIR investigations of various montmorillonite clays modified by monocationic and dicationic imidazolium ionic liquids, J. Mol. Struct. 1173 (2018) 653–664.
[32] J.-M. Negrete, J. Letoffe, L. Putaux, L. David, E. Bourgeat-Lami, Aqueous dispersions of silane-functionalized laponite clay platelets. A first step toward the elaboration of water-based polymer/clay nanocomposites, Langmuir 20 (2004) 1564–1571.
[33] M. Huskić, M. Žigon, M. Ivanković, Comparison of the properties of clay polymer nanocomposites prepared by montmorillonite modified by silane and by quaternary ammonium salts, Appl. Clay Sci. 85 (2013) 109–115.
[34] J. Berriot, H. Montes, F. Lequeux, D. Long, P. Sotta, Evidence for the shift of the glass transition near the particles in silica-filled elastomers, Macromolecules 35 (2002) 9756–9762.
[35] H. Montes, F. Lequeux, J. Berriot, Influence of the glass transition temperature gradient on the nonlinear viscoelastic behavior in reinforced elastomers, Macromolecules 36 (2003) 8107–8118.
[36] Y. Fukahori, New progress in the theory and model of carbon black reinforcement of elastomers, J. Appl. Polym. Sci. 95 (2005) 60–67.
[37] S. Sadhu, A.K. Bhowmick, Effect of nanoclay on the dynamic mechanical properties of styrene butadiene and acrylonitrile butadiene rubber vulcanizates, Rubber Chem. Technol. 78 (2005) 321–335.
[38] B. Read, G. Williams, Analysis of curves of loss factor against reciprocal temperature for dielectric and dynamic mechanical relaxation, Trans. Faraday Soc. 57 (1961) 1979–1987.
[39] M.C.O. Chang, D.A. Thomas, L.H. Sperling, Characterization of the area under loss modulus and tan δ–temperature curves: acrylic polymers and their sequential interpenetrating polymer networks, J. Appl. Polym. Sci. 34 (1987) 409–422.
[40] S. Mortazavian, A. Fatemi, Effects of fiber orientation and anisotropy on tensile strength and elastic modulus of short fiber reinforced polymer composites, Compos. B Eng. 72 (2015) 116–129.
[41] J. Zhang, L. Wang, Y. Zhao, Improving performance of low-temperature hydrogenated acrylonitrile butadiene rubber nanocomposites by using nano-clays, Mater. Des. 50 (2013) 322–331.
[42] H. Bouasse, Z. Carrière, Sur les courbes de traction du caoutchouc vulcanisé, Annales de la Faculté des sciences de Toulouse: Mathématiques, 1903, pp. 257–283.
[43] L. Mullins, Softening of rubber by deformation, Rubber Chem. Technol. 42 (1969) 339–362.
[44] J. Diani, B. Fayolle, P. Gilormini, A review on the Mullins effect, Eur. Polym. J. 45 (2009) 601–612.
[45] L. Mullins, Effect of stretching on the properties of rubber, Rubber Chem. Technol.

21 (1948) 281–300.
[46] G. Kraus, C.W. Childers, K.W. Rollmann, Stress softening in carbon black-reinforced vulcanizates. Strain rate and temperature effects, J. Appl. Polym. Sci. 10 (1966) 229–244.
[47] D.E. Hanson, M. Hawley, R. Houlton, K. Chitanvis, P. Rae, E.B. Orler, D.A. Wrobleski, Stress softening experiments in silica-filled polydimethylsiloxane provide insight into a mechanism for the Mullins effect, Polymer 46 (2005) 10989–10995.
[48] L. Yan, D.A. Dillard, R.L. West, L.D. Lower, G.V. Gordon, Mullins effect recovery of a nanoparticle-filled polymer, J. Polym. Sci. B Polym. Phys. 48 (2010) 2207–2214.
[49] S. Cantournet, R. Desmorat, J. Besson, Mullins effect and cyclic stress softening of filled elastomers by internal sliding and friction thermodynamics model, Int. J. Solids Struct. 46 (2009) 2255–2264.
[50] A. Sreeram, N.G. Patel, R.I. Venkatanarayanan, J.B. McLaughlin, S.J. DeLuca, P.A. Yuya, S. Krishnan, Nanomechanical properties of poly(*para*-phenylene vinylene) determined using quasi-static and dynamic nanoindentation, Polym. Test. 37 (2014) 86–93.
[51] S.-J. Park, K.-S. Kim, A. Mendez-Vilas, J. Diaz, Surface Characterization of Carbon Materials by X-Ray Photoelectron Spectroscopy, Microscopy: Science, Technology, Applications and Education, Formatex, (2010), pp. 1905–1916.

Enhanced elastomer toughness and fracture properties imparted by chemically reactive flat nanoparticles

Supplementary Data

Malavarayan Sankarasubramanian[a,b,e,§], Monavareh Torabizadeh[c,§], Zackary A. Putnam[a,b], John C. Moosbrugger[c], Ming Y. Huang[d], Sitaraman Krishnan,[a,*]

[a] *Department of Chemical & Biomolecular Engineering, Clarkson University, Potsdam, NY 13699, USA*
[b] *Materials Science & Engineering Ph.D. Program, Clarkson University, Potsdam, NY 13699, USA*
[c] *Department of Mechanical &Aeronautical Engineering, Clarkson University, Potsdam, NY 13699, USA*
[d] *Baker Hughes, a GE Company, Houston, TX 77073, USA*
[e] *Presently at Intel Corporation, Chandler, AZ 85226, USA*

* Corresponding author. E-mail address: skrishna@clarkson.edu
[§] These authors contributed equally.

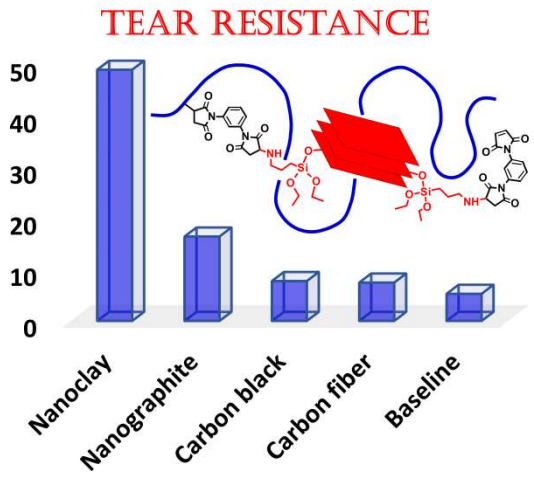

The incorporation of flat (2-dimensional) clay nanoparticles in HNBR elastomer resulted in a several-fold improvement in tear resistance compared with spherical carbon black. The surface-functionalized clay nanoparticles, capable of forming particle–particle and particle–polymer interfacial bonds, also imparted other desirable properties such as high stiffness, ductility, toughness, and crack initiation resistance.

https://doi.org/10.1016/j.polymertesting.2019.105932

Thermogravimetric analysis of surface-functionalized clay particles

Fig. S1 shows the thermogravimetric and differential thermogravimetric (DTG) results for the surface-functionalized nanoclay, Nanomer I.31 PS, acquired using a Perkin Elmer Pyris 100 thermogravimetric analyzer. A total mass loss of approximately 30 wt % was observed at a temperature of 900 °C. Three different steps of mass loss could be discerned, consistent with the observations of Asgari et al. [1] for other organofunctionalized clays. Curve fitting of the DTG results indicated that up to about 37 % of the organic groups were relatively weakly bound to the clay particles and could be released over a temperature range of 200 to 500 °C. The remaining organic content of the clay was strongly bound, either because of intercalation or chemical grafting.

Calculation of activation energy of glass transition

The activation energy of glass transition, Q, was determined using Eq. (S1).

$$Q = \frac{-2.303(\log_{10} E'_G - \log_{10} E'_R)\pi R}{2\int_{T_G}^{T_R} \tan\delta \, \mathrm{d}\left(\frac{1}{T}\right)} \tag{S1}$$

$\log_{10} E'_G$ and $\log_{10} E'_R$, corresponding to temperatures T_G and T_R, were determined from the plot of the logarithm of storage modulus, E', vs. T. The integral of $\tan\delta$ with respect to $1/T$ was determined after subtracting a linear baseline from the $\tan\delta$ vs. T plot. Consistent with the observation of Fey et al. [2], the activation energy calculated using Eq. (S1) is sensitive to the choice of the baseline and the limits of integration. A range of $T_g - 50$ to $T_g + 50$ was chosen.

Fig. S2(a) shows a plot of $\log_{10} E'$ vs. T, wherein the temperatures corresponding to the onset and conclusion of glass transition, T_G and T_R, are marked along with the corresponding storage modulus values, $\log_{10} E'_G$ and $\log_{10} E'_R$, respectively. Fig. S2(b) shows a plot of $\tan\delta$ vs. T along with the linear baseline, used for finding the peak area. Fig. S2(c) shows the $\tan\delta$ vs. T data after baseline subtraction. Fig. S2(d) shows a plot of $\tan\delta$ vs. $1/T$, the area under which was determined for the calculation of Q. Fig. S3 shows a similar set of plots for the clay-filled NC45 elastomer.

Cyclic tensile testing

Fig. S4 shows the results of cyclic tensile testing of the graphite-filled NG45 elastomer. The plots for CF45-PARL, CF45-PERP, and BASE elastomers are shown in Figs. S5, S6, and S7, respectively. Fig. S8 shows the dissipated energy fraction for all the elastomers of the present study.

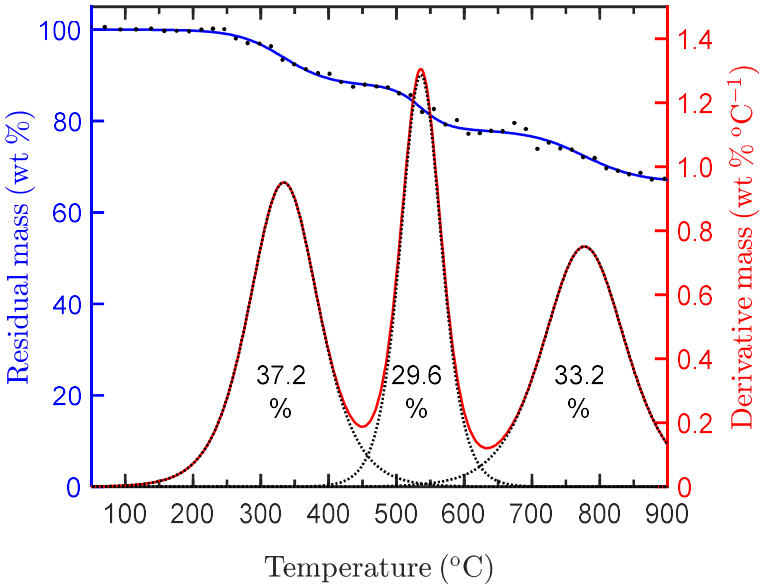

Fig. S1. Thermogravimetry and differential thermogravimetry results for surface-functionalized clay filler particles; sample heated up to 900 °C at a rate of 10 °C min^{-1} under 20 cm^3 min^{-1} argon purge, after holding at 50 °C for 5 min at the start of the experiment.

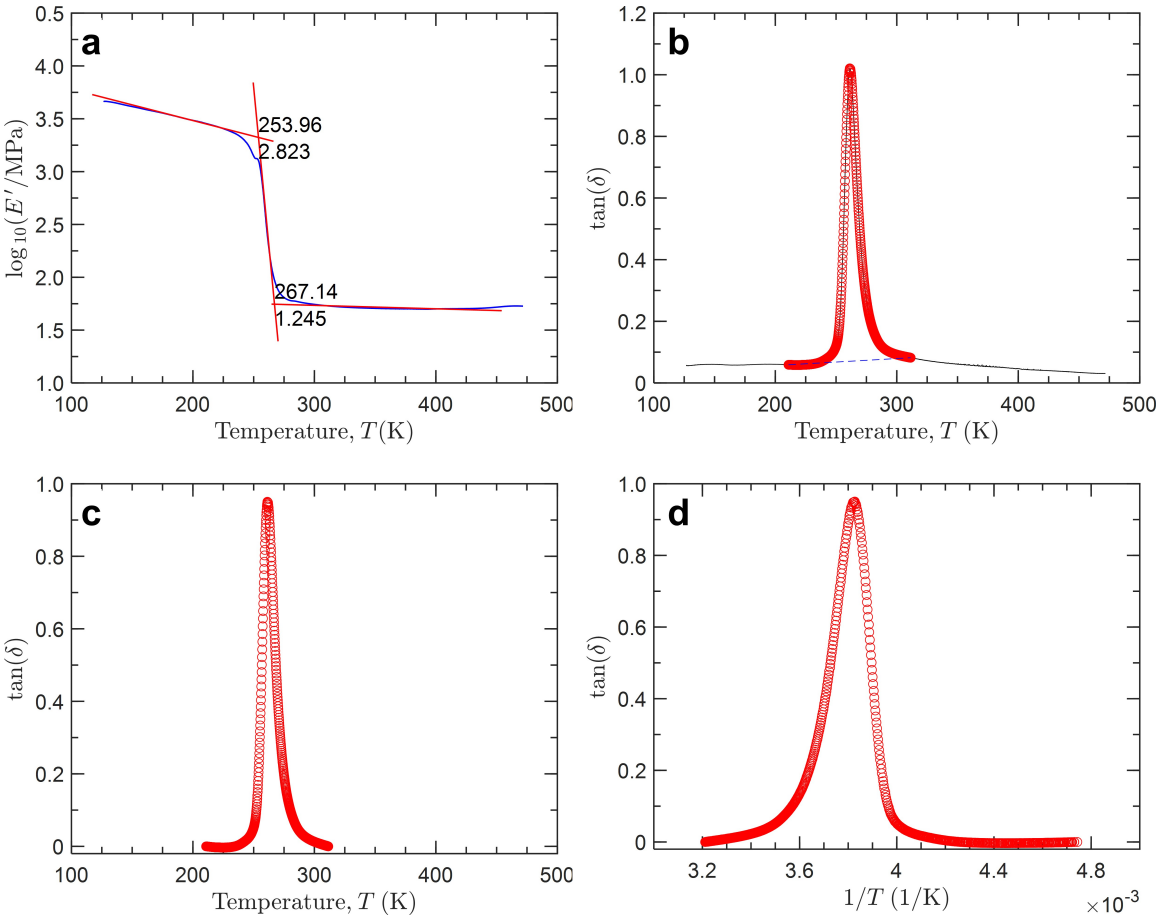

Fig. S2. Determination of activation energy of glass transition for the CB45 elastomer.

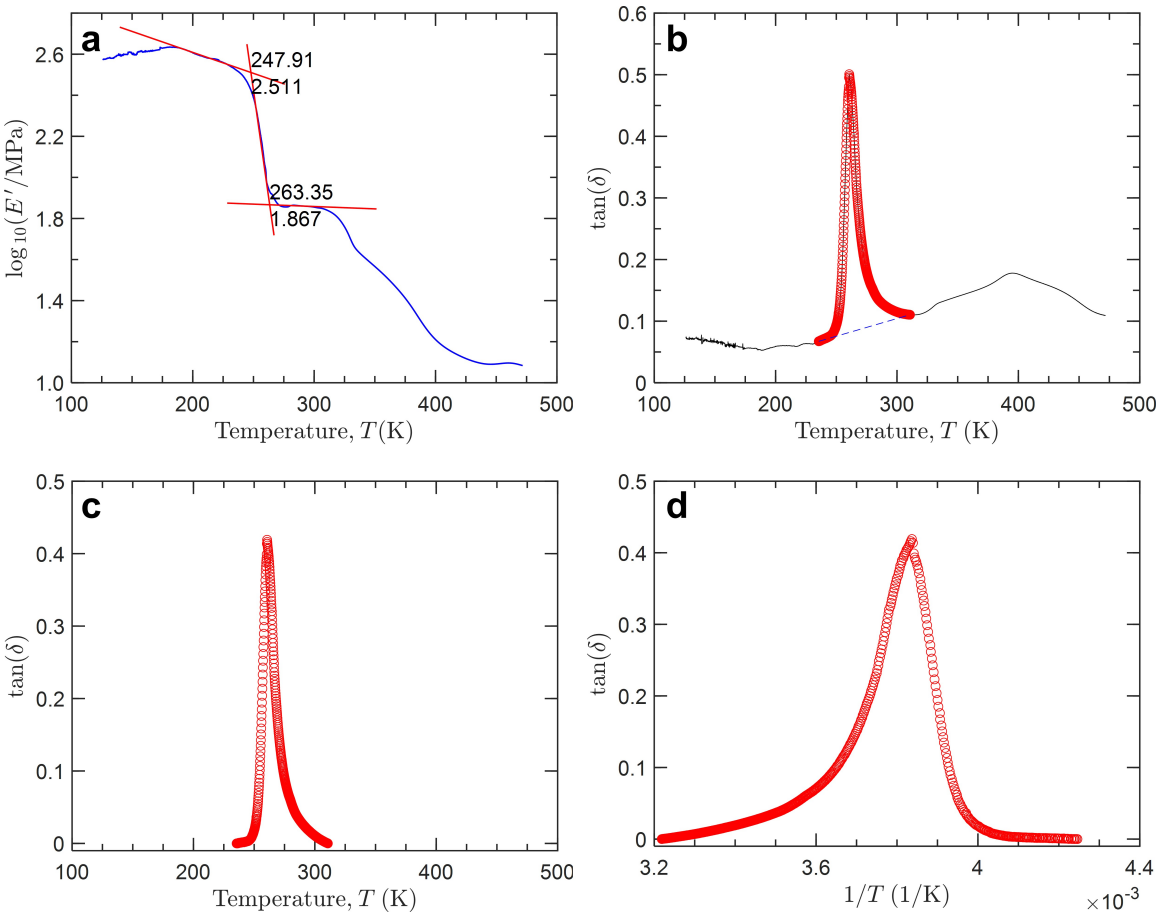

Fig. S3. Determination of activation energy of glass transition for the NC45 elastomer.

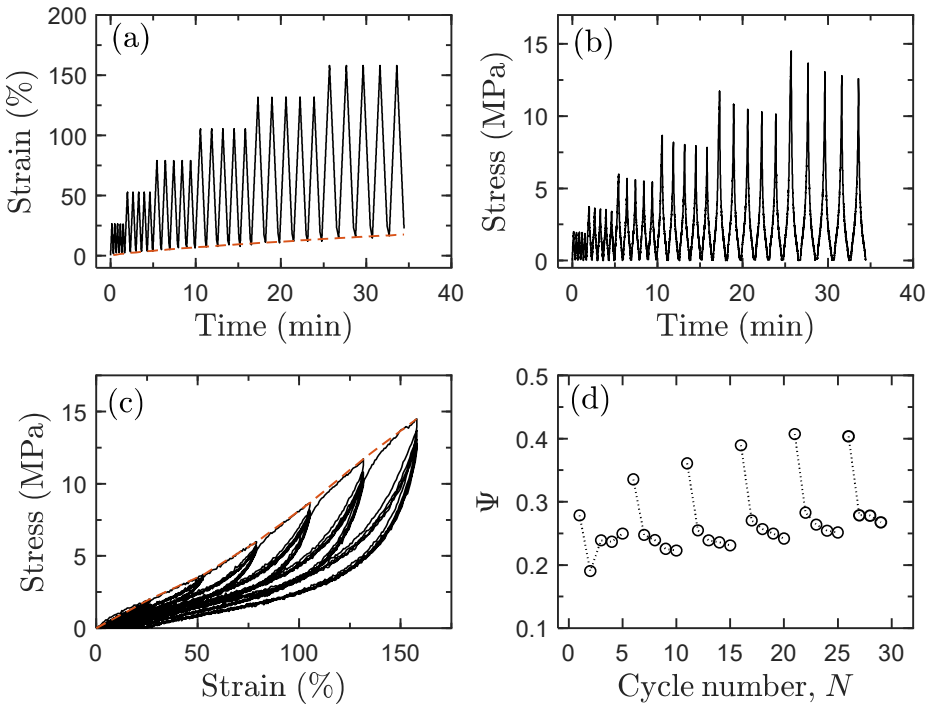

Fig. S4. Cyclic tensile testing results for NG45 at room temperature: (a) engineering strain vs. time; (b) engineering stress vs. time; (c) stress vs. strain; and (d) dissipated energy fraction vs. cycle number.

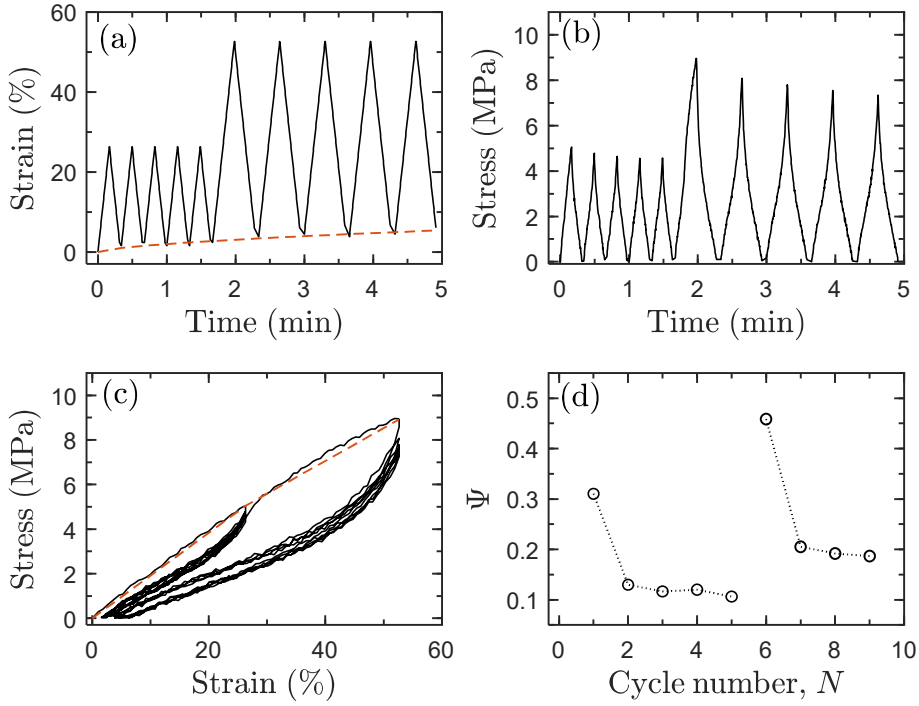

Fig. S5. Cyclic tensile testing results for CF45-PARL at room temperature: (a) engineering strain vs. time; (b) engineering stress vs. time; (c) stress vs. strain; and (d) dissipated energy fraction vs. cycle number.

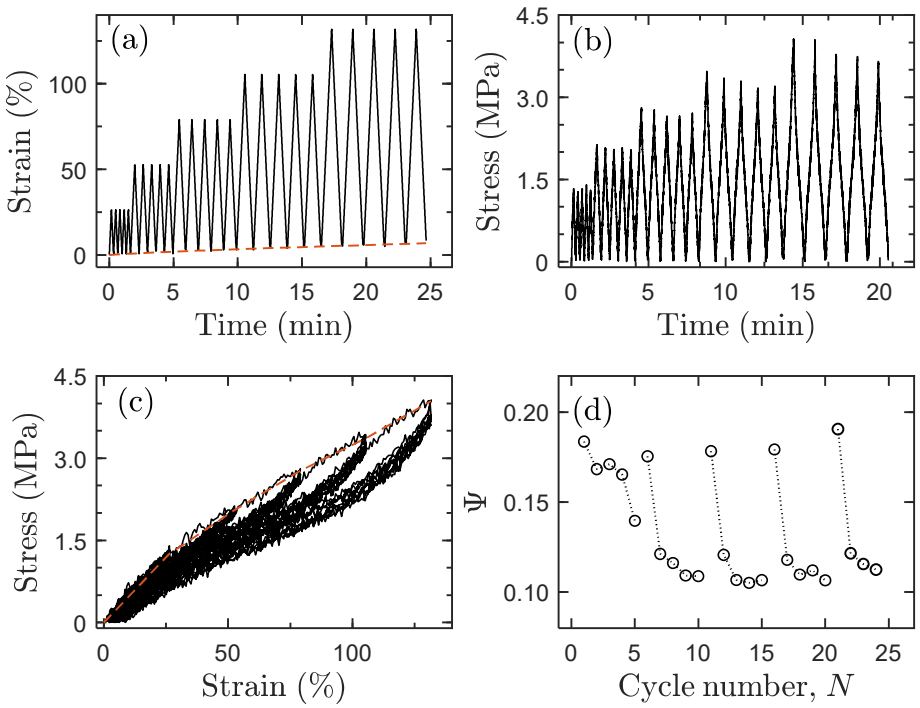

Fig. S6. Cyclic tensile testing results for CF45-PERP at room temperature: (a) engineering strain vs. time; (b) engineering stress vs. time; (c) stress vs. strain; and (d) dissipated energy fraction vs. cycle number.

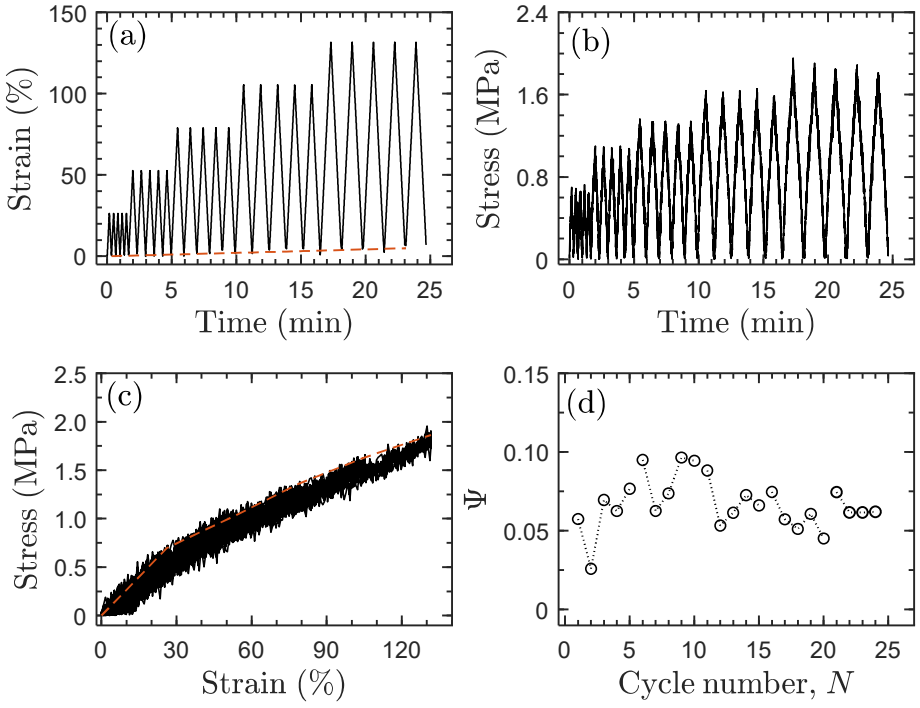

Fig. S7. Cyclic tensile testing results for the unfilled elastomer at room temperature: (a) engineering strain vs. time; (b) engineering stress vs. time; (c) stress vs. strain; and (d) dissipated energy fraction vs. cycle number.

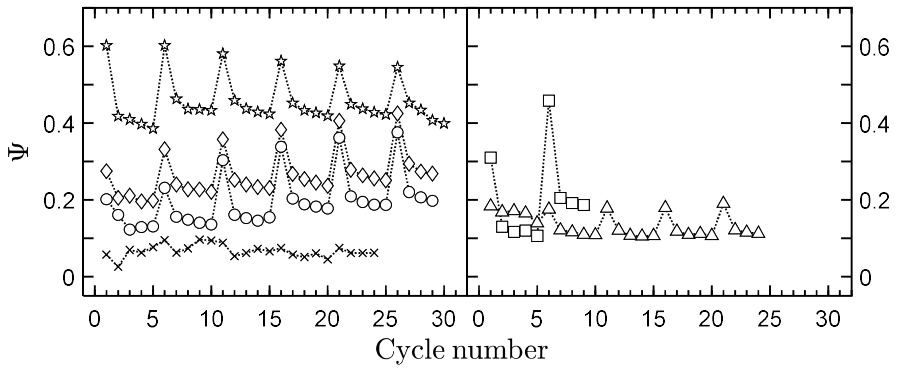

Fig. S8. Dissipated energy fraction vs. cycle number: NC45 (☆), NG45 (◇), CB45 (○), BASE (×), CF45-PARL (□), CF45-PERP (△).

References

[1] M. Asgari; A. Abouelmagd; U. Sundararaj, Silane functionalization of sodium montmorillonite nanoclay and its effect on rheological and mechanical properties of HDPE/clay nanocomposites, Applied Clay Science, 146 (2017) 439−448.

[2] J. Fay, D. Thomas, L. Sperling, valuation of the area under linear loss modulus-temperature curves, Journal of Applied Polymer Science, 43 (1991) 1617−1623.